ACS APPLIED MATERIALS & INTERFACES

Research Article

www.acsami.org

Molecular Weight Dependence of the Morphology in P3HT:PCBM Solar Cells

Feng Liu,[†] Dian Chen,[†] Cheng Wang,[‡] Kaiyuan Luo,[§] Weiyin Gu,[†] Alejandro L. Briseno,[†] Julia W. P. Hsu,[§] and Thomas P. Russell*,[†]

[†]Department of Polymer Science and Engineering, University of Massachusetts, Amherst, Massachusetts 01003, United States
[‡]Advanced Light Source (ALS), Lawrence Berkeley National Laboratory (LBNL), Berkeley, California 94720, United States
[§]Department of Materials Science and Engineering, University of Texas at Dallas, Richardson, Texas 75080, United States

Supporting Information

ABSTRACT: In polymer-based photovoltaic devices, optimizing and controlling the active layer morphology is important to enhancing the device efficiency. Using poly(3-hexylthiophene) (P3HT) with well-defined molecular weights (MWs), synthesized by the Grignard metathesis (GRIM) method, we show that the morphology of the photovoltaic active layer and the absorption and crystal structure of P3HT are dependent on the MW. Differential scanning calorimetry showed that the crystallinity of P3HT reached a maximum for intermediate MWs. Grazing-incidence wide-angle X-ray diffraction showed that the spacing of the (100) planes of P3HT increased with increasing MW, while the crystal size decreased. Nonlinear crystal lattice expansions were found for both the (100) and (020) lattice planes, with an unusual $\pi-\pi$-stacking enhancement observed between 50 and 100 °C. The melting point depression for P3HT, when mixed with [6,6]-phenyl-C61-butyric acid methyl ester (PCBM), and, hence, the Flory–Huggins interaction parameter depended on the MW. PCBM was found to perturb the ordering of P3HT chains. In photovoltaic devices, P3HT with a MW of ∼20K showed the best device performance. The morphologies of these blends were studied by grazing-incidence small-angle X-ray scattering (GISAXS) and resonant soft X-ray scattering. In GISAXS, we observed that the low-molecular-weight P3HT more readily crystallizes, promoting a phase-separated morphology.

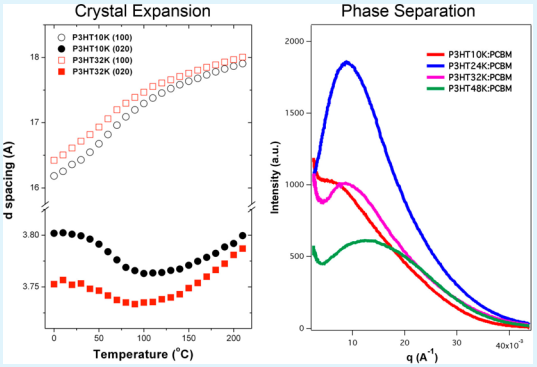

KEYWORDS: *P3HT, morphology, molecular weight, melting point depression, crystallinity*

1. INTRODUCTION

Bulk heterojunction (BHJ)-type organic photovoltaic (OPV) solar cells consisting of a light-harvesting conjugated polymer (donor) and an electron-accepting fullerene derivative (acceptor) afford efficient thin-film solar cell devices.[1,2] Within BHJ OPVs, a bicontinuous morphology, comprised of an intermixing of donor and acceptor phases, is necessary for the transport of electrons and holes to their respective electrodes.[3−5] The characteristic length scales of the domains comprising this morphology must be commensurate with the exciton diffusion length (∼10 nm), so as to minimize recombination of the bounded electron–hole pairs and maximize the interfacial area where charge separation occurs.[6] The performance of BHJ OPV-based solar cells depends strongly on the absorption properties of the donor polymer and the morphology of the blended active layer. It remains a challenge to maximize photon absorption, charge separation, and charge transport, while maintaining the necessary size scale and bicontinuity of the BHJ morphology.[7] The morphology of the active layer, sandwiched between two electrodes, is strongly dependent on the preparation conditions, including the choice of solvent,[8,9] the rate of solvent removal,[10−12] the use of chemical additives,[13−19] thermal annealing treatments,[20−24] and solvent annealing conditions.[25−28] The performance is also affected by the intrinsic properties of the light-harvesting polymers, for example, the molecular weight (MW) and polydispersity index (PDI).[29−38] There have been several studies that correlate the device performance and MW. Yet, previous work has been limited by either the quality of the materials or the methods of characterization.[30−32] In this work, we synthesized a series of poly(3-hexylthiophene)s (P3HTs) with controlled MW and PDI as model systems to study their physical properties as well as the morphology of their mixtures with [6,6]-phenyl-C61-butyric acid methyl ester (PCBM). OPV devices were fabricated, and the active layer morphologies with different annealing treatment conditions are analyzed to correlate with the device performance.

Received: August 7, 2014
Accepted: October 28, 2014
Published: October 28, 2014

2. RESULTS AND DISCUSSION

2.1. Physical Properties of Polymers. P3HTs with different MWs were synthesized by the Grignard metathesis (GRIM) method.[39] The MW was controlled by varying the monomer/catalyst ratio. Soxhlet extraction was used to remove the low-MW polymers. Size-exclusion chromatography was used to characterize the MW and PDI using polystyrene as a standard (Figure S1 in the Supporting Information, SI). Well-defined peaks with different elution times were observed. The regioregularity (RR) was determined by ^{1}H NMR, using the method described by Fréchet and co-workers.[40] It has to be noted that the GRIM P3HT synthesis will always have a defect of RR for each chain at the beginning. The RRs reported were corrected for this defect, as described by McCullough and co-workers.[41] Table 1 summarizes the characteristics of the different P3HTs (MWs from 5K to 48K with PDIs from 1.2 to 1.4 and RRs from 94 to 96%, respectively) used in this study.

Table 1. Physical Properties of P3HTs

	P3HT1	P3HT2	P3HT3	P3HT4	P3HT5
M_n (Da)[a]	4.6K	9.6K	23.8K	32.3K	48.0K
PDI[b]	1.3	1.3	1.2	1.3	1.4
DP[c]	25	50	120	200	375
RR (%)[d]	94	95	96	96	96
T_m (°C)	171	211	230	234	234
HOMO (eV)	4.68	4.67	4.64	4.65	4.64

[a]M_n is the number-average molecular weight. [b]PDI is the ratio of the weight to M_n. [c]DP is the degree of polymerization. [d]RR is the regioregularity.

2.1.1. Optical Properties. Figure 1a shows the absorption profiles of the different P3HT thin films after spin coating from chlorobenzene. All of the samples showed spectral tails extending to 700 nm. For the low-MW P3HT5K, the absorption maximum is located at 515 nm and the shoulder at 605 nm is weaker when compared to the high-MW polymers. For polymers with MW > 10K, the absorption profiles are similar, with a main peak at 560 nm and a shoulder at 605 nm, indicating that the effective main-chain conjugation length saturates. The blue shift in P3HT5K suggests that it is less ordered compared to that of the higher-MW samples,[42] which is in keeping with the change in the (100) spacing discussed below. A smaller (100) d spacing is observed in the P3HT5K sample, making this crystal packing different from that observed for the higher-MW samples. The structure model of P3HT shows that alkyl side chains are tilted with respect to the polythiophene backbone without interdigitation,[43] A reduced spacing in P3HT5K indicates that there might be some disorder of alkyl side chains, leading to disorder in its crystals. This is supported by the transmission X-ray diffraction results, where a slightly greater $\pi-\pi$-stacking distance for the lower-MW P3HTs is observed. This may give rise to the low melting enthalpy and different light absorption. By annealing the films for 5 min at 150 °C, the orange color of the as-spun film changed to red-purple. This is reflected in the observed enhancement of the 605 nm shoulders in Figure 1b. The 605 nm shoulder has been attributed to the interchain stacking, which is related to the packing of adjacent P3HT chains. In annealed samples, the ordering was found to decrease with increasing MW; i.e., the intensity of 605 nm shoulder decreased for P3HT with MW from 24K to 48K, as seen from Figure S2 in the SI. This reduction in the interchain ordering may be attributed to a reduction in the mobility (increase in the viscosity) or an increase in the chain entanglements with increasing MW, which will slow the rate of the ordering during annealing. The chain length of P3HT will also influence the characteristics of any aggregation in solution, particularly in relatively poor solvents (Figure 1c). P3HTs were dissolved in chloroform (~1 mg/mL), and then by the addition of a small amount of acetone (chloroform:acetone = 9:1 volume ratio), a poor solvent for P3HT, the polymer chains began to aggregate. With increasing MW, stronger aggregation occurred. For P3HT48K, the absorption characteristic of aggregation becomes stronger than the 450 nm absorption band.

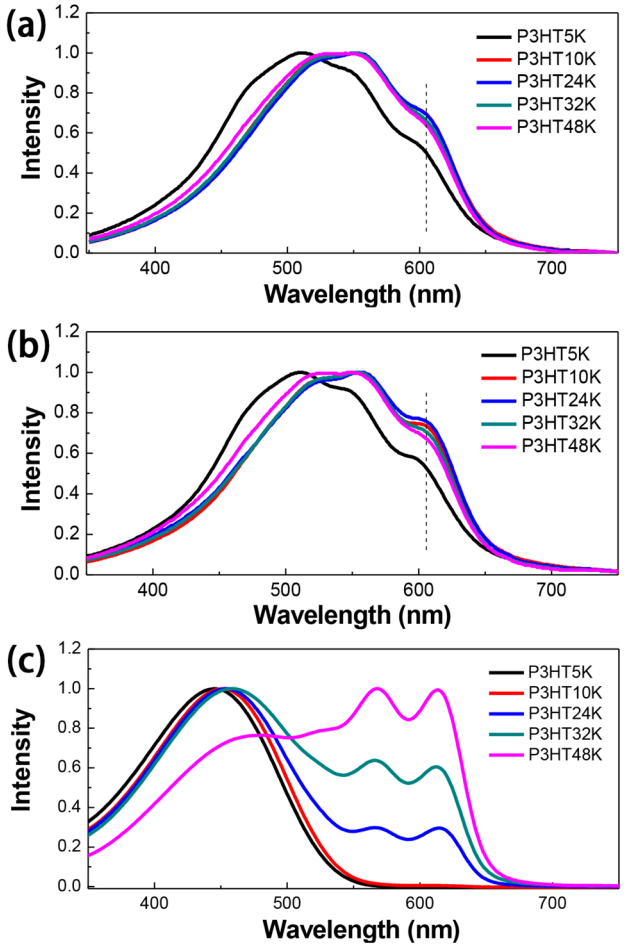

Figure 1. Absorption of a spin-cast thin film from a chlorobenzene solution: (a) as-spun thin film; (b) annealed thin film; (c) absorption of P3HT aggregates in a mixed solvent.

2.1.2. Electronic Properties. Both the MW of the conjugated polymer and packing in the thin film influence the electronic structure of the material. This effect was studied by comparing the ionization potential, which is the highest occupied molecular orbital (HOMO), of the polymers. The HOMO of solid-state P3HT thin films was studied by photoelectron emission spectroscopy in air (PESA),[44,45] with data summarized in Figure 2. In the low-MW region (5K–20K), the HOMO energy level decreases as the MW increases. When the MW is greater than 24K, the HOMO energy level becomes relatively constant, around 4.64–4.65 eV. The HOMO energy level for a donor polymer is quite important because it largely determines the open-circuit voltage (V_{oc}) of the solar cell devices. Thus, we expect a larger V_{oc} for the low-MW P3HTs.

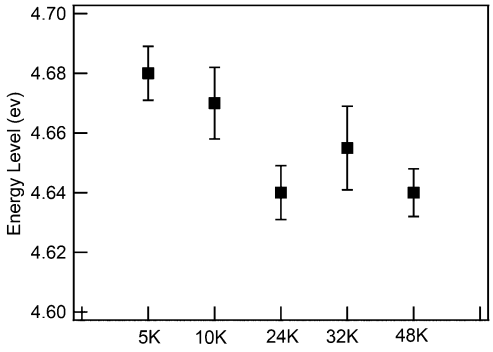

Figure 2. HOMO energy levels of P3HTs measured by the PESA method.

2.1.3. Thermal Properties. Differential scanning calorimetry (DSC) was used to evaluate the thermal properties of P3HT as a function of the MW. Shown in Figure 3a are the second heating traces (10 °C/min rate) of the different MW P3HT samples. Initially, with increasing MW, the melting point of P3HT increased. When the MW is more than 24K, the melting point remains constant. Both chain packing and crystal size influence the melting point. A similar melting point for high-MW P3HTs indicates that their packing and crystal size are similar (shown subsequently). The enthalpy of fusion, ΔH_f, as calculated from the area under the endotherm, is shown in Figure 3b, where it is seen that, with increasing MW, a maximum is observed, which indicates that the degree of crystallinity of the polymers reaches a maximum at intermediate

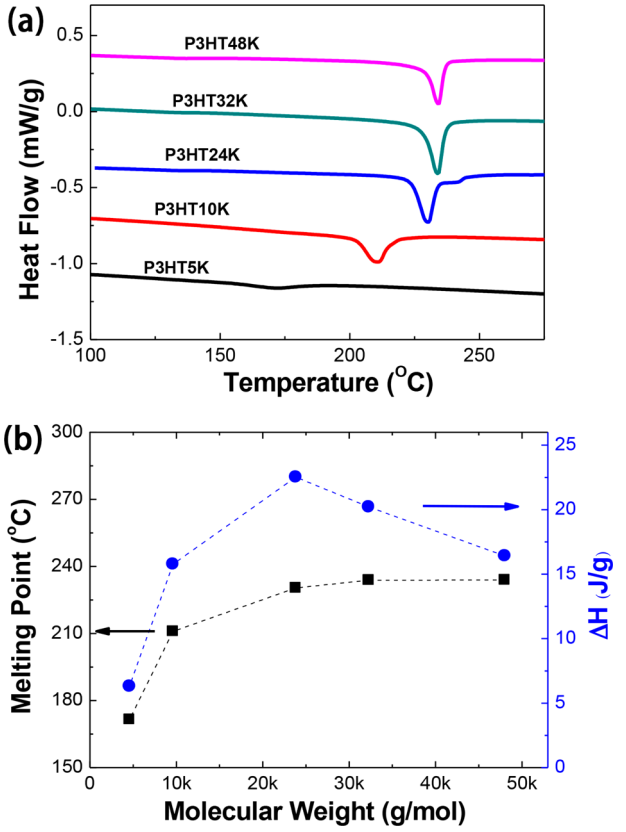

Figure 3. (a) Second DSC heating traces of different MW P3HTs with a heating rate of 10 °C/min. (b) Summarized melting point and heat of fusion of P3HTs from second heating traces.

MWs. Malik and Nandi reported a $\Delta H°_f$, the heat of fusion for 100% crystalline P3HT, of 99 J/g.[46] Using this value, the degree of crystallinity, calculated from $\Delta H_f/\Delta H°_f$, for the P3HTs used in our studies ranges from 6.4 to 22.8%, with P3HT5K showing the lowest value, which is consistent with the optical data shown in Figure 1. It should also be noted that other reports obtained other values of $\Delta H°_f$; however, those values will not change the trend of the crystallinity for our MW P3HT except the absolute crystallinity. A decrease in ΔH_f with decreasing MW (from 24K to 5K) was also observed by Zen et al.,[35] but as shown, this trend is not monotonic over a wider MW range. The decrease in the crystallinity with increasing MW (from 24K to 48K) can be attributed to an increase in the viscosity or chain entanglements of the melt, which would reduce the crystallization kinetics. The increase in the crystallinity from 5K to 24K can be attributed to an increase in the order or perfection of the P3HT crystals, as evidenced by the change in the (100) spacing, as discussed below.

2.1.4. Structure Properties. Grazing-incidence wide-angle X-ray diffraction (GIXD) was used to assess the ordering of P3HT in thin films. Figure 4a shows the out-of-plane scattering profile, i.e., normal to the film surface, of annealed P3HT thin films. For all samples, a well-defined (100) reflection is observed, along with second-order (200) and third-order (300) reflections. No obvious (020) peak is observed. This result indicates that the polymer chains adopt an edge-on orientation in the film. For P3HT5K, the reflections are stronger and sharper than those of the other samples, suggesting that P3HT5K can be more readily oriented in thin films than the higher-MW materials. The (100) *d* spacing of P3HT, shown in Figure 4b, is found to increase from ~1.63 nm for P3HT5K to 1.69 nm for P3HT24K and then remain

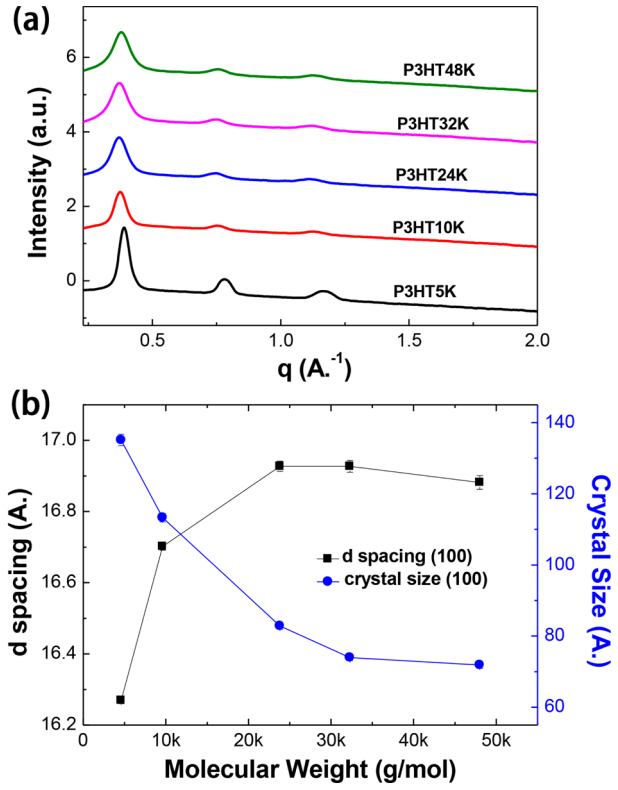

Figure 4. (a) GIXD of pure P3HT and in the out-of-plane direction. (b) (100) *d*-spacing and crystal-size analysis of a P3HT thin film.

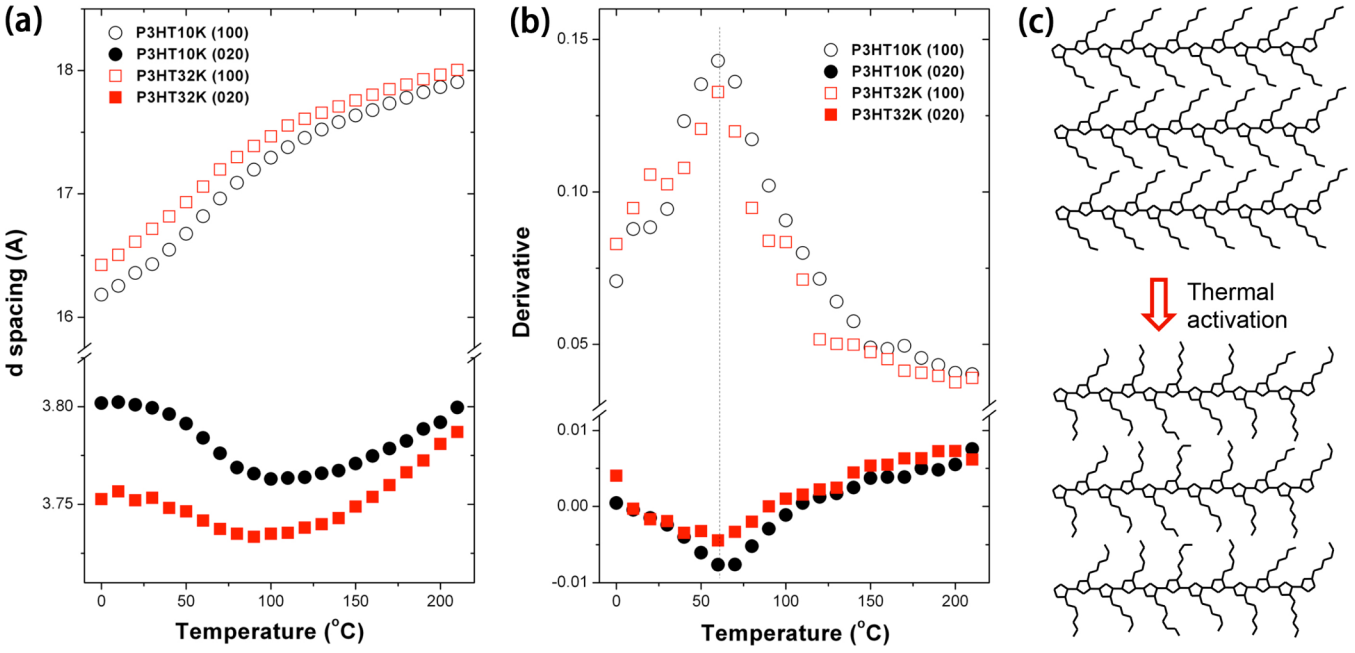

Figure 5. (a) (100) and (020) *d* spacing of pure P3HT. (b) First derivative of *d* spacing. (c) Proposed side-chain disordering of P3HT during heating.

constant with a further increase in the MW. This is in keeping with the findings of Zen et al.[35] The reduction of the spacing in the P3HT5K sample suggests there might be a disordering of the side chains in the solid-state packing.[43] Using Scherrer analysis,[47] the persistence of the crystal along the (100) direction (Figure 4b) is seen initially to decrease sharply with increasing MW up to 24K and then remain constant. These results, together with the optical and thermal properties, suggest that medium-MW P3HT (~24K) is a turning point for their physical properties.

Temperature-dependent transmission wide-angle X-ray scattering (WAXS) measurements were carried out on bulk P3HT samples to elucidate the lattice expansion for P3HT crystals (Figure S3 in the SI). The *d* spacing and temperature relationship are plotted in Figure 5. Although the (100) spacing is larger for higher-MW P3HT, it has a slightly smaller (020) spacing. For the (100) crystal plane, a continuous expansion is observed upon annealing. An inflection is observed around 100 °C, below which the expansion coefficient is much larger. These results indicate that, although the melting point for P3HT is above 200 °C, the internal structure of the crystal changes at ~100 °C. More surprisingly, the (020) crystal plane undergoes a nonlinear thermal expansion. When the temperature is lower than 30 °C, no obvious lattice parameter change is observed. Increasing the temperature further, a decrease in the *d* spacing is observed between 30 and 100 °C. Further heating leads to the expansion of the (020) stacking. Bearing in mind that the (100) direction reflects the separation of the main chain separated by the alkyl side chains and the (020) direction is along the $\pi-\pi$-stacking direction, a larger thermal expansion coefficient below 100 °C indicates that there are certain collective effects that expand the lattice spacing, which is related to the introduction of more gauche conformations in the side chains that lead to an increase in the (100) direction (see Figure 5c). Because of this relaxation, a slight reorganization of the backbone is enabled. Thus, the $\pi-\pi$ interactions drive the system to achieve a better interfacial stacking, as shown in the reduction in the (020) distance. The first derivative of the expansion of the crystal is shown in Figure 5b, which gives a maximum and a minimum for the (100) and (020) crystal planes at ~60 °C, in keeping with the side-chain melting of P3HT seen in the DSC and IR measurements,[48] further supporting this argument. Below this temperature, both material expansion and structure change (side-chain melting) add up to deliver a large thermal expansion coefficient. Above this temperature, material expansion dominates the thermal expansion coefficient, with a reduced value.

In GIXD, the azimuthal dependence of the diffraction arcs reflects the orientation of the crystal planes. The normalized orientation distribution function (ODF) of the reciprocal lattice vectors and their second moments were determined to evaluate the crystal orientation (see the SI for details).[49] Parts a and b of Figure 6 show the ODF of (100) scattering arcs for annealed P3HT and P3HT:PCBM blends (here the annealing is "preannealing", that is, direct annealing of the P3HT:PCBM blends before electrode deposition) under the same conditions. Figure 6c shows the (100) orientation factor. For pure P3HT, the orientation seen for P3HT5K at ~0.6 then decreases to 0.4 for P3HT10K and remains constant with increasing MW. This result shows an interesting property of low-MW P3HT, where the chains orient more readily. With the addition of PCBM, the trends are the same but there is a marked decrease in the orientation. In fact, for MWs of 10K or higher, there is very little orientation.

2.1.5. Interaction with PCBM. Before fabrication of the solar cell devices, the miscibilities of P3HT and PCBM were investigated. Melting point depression studies were performed to evaluate the interaction parameter, χ, between P3HT and PCBM, following the polymer and diluent mixture melting point depression theory.[50−53] Mixtures of PCBM in P3HT (2−20 wt %) were prepared, and the melting point was measured by DSC.[52] Details of the sample preparation and experimental procedure are described in the SI.

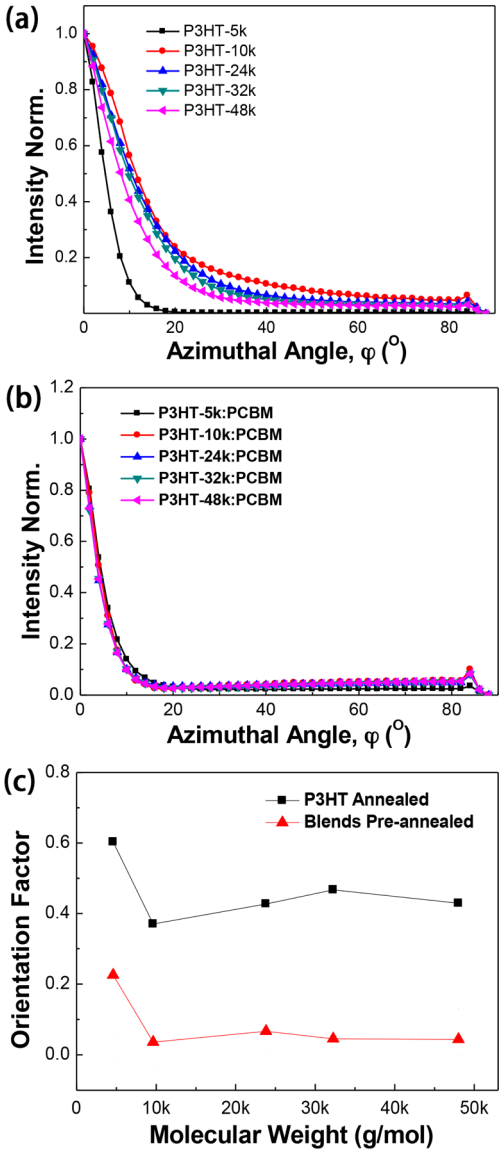

Figure 6. (a) ODF for the out-of-plane (100) diffraction peak of a pure annealed P3HT thin film. (b) ODF for the out-of-plane (100) diffraction peak of an annealed P3HT:PCBM blend thin film. (c) Orientation factors of the out-of-plane (100) diffraction.

$$\frac{1}{T_m} - \frac{1}{T_m^\circ} = \frac{RV_{2u}}{\Delta H_{2u} V_1}[\phi_1 - \chi_{12}\phi_1^2] \quad (1)$$

Equation 1 describes the melting point depression due to mixing of a crystalline polymer and with a low-MW diluent (PCBM). The subscript 1 denotes the diluent and 2 the crystalline polymer. T_m° is the melting point of pure P3HT obtained using the same procedure. ϕ is the volume fraction, V is the molar volume of the repeat unit, χ_{12} is the Flory–Huggins segmental interaction parameter, and R is the ideal gas constant. Because χ_{12} is defined as

$$\chi_{12} = \frac{BV_1}{RT} \quad (2)$$

where V_1 is the molar volume of the diluent and B represents the interaction energy density characteristic of the solvent–solute pair. By substituting eq 2 into eq 1, we obtain

$$\frac{1}{\phi_1}\left[\frac{1}{T_m} - \frac{1}{T_m^\circ}\right] = \frac{RV_{2u}}{\Delta H_{2u} V_1}\left[1 - \frac{BV_1}{R}\frac{\phi_1}{T_m}\right] \quad (3)$$

When $(1/\phi_1)(1/T_m - 1/T_m^\circ)$ is plotted as a function of ϕ_1/T_m, BV_1/R can be obtained from the ratio of the slope/intercept. A significant melting temperature depression was observed for P3HT blended with different amounts of PCBM. Figure 7a shows plots of $(1/\phi_1)(1/T_m - 1/T_m^\circ)$ as a function of ϕ_1/T_m for different MWs of P3HTs. The calculated values of χ_{12} for PCBM and P3HT at 150 °C are shown in Figure 7b. As can be seen, χ_{12} increases from ~0.2 to 0.4 with increasing MW as the melting point increases from 172 to 234 °C. Because the repeating unit of P3HT is, of course, independent of the MW, the increase in χ_{12} or decrease in the miscibility with increasing MW may arise from a decrease in the number of end groups or chain ends, which decreases from 2:25 for the P3HT5K polymer to 2:375 for P3HT48K. For all MWs, $\chi_{12} < 0.5$ indicates that, at the melting point of P3HT, P3HT and PCBM are miscible. This also supports the argument that the origin of the phase-separated morphology is not demixing but rather from segregation of PCBM forced by the ordering of P3HT, as discussed in our previous studies.[22,54] In fact, we observed that prolonged thermal annealing of P3HT:PCBM blends will lead to a macroscopic phase separation of the two components caused by PCBM organization. Figure 7c shows the optical microscopic images of a blended thin film annealed in 150 °C for 30 min. Rod-shaped aggregates are evident in the micrographs, as shown by us and others previously,[55] and have been shown to be PCBM that has crystallized. From P3HT10K to P3HT48K, the PCBM agglomerate density increases. P3HT5K does not show many agglomerates, indicating a better miscibility between the polymer and PCBM, which is due to the smaller χ. From P3HT24K to P3HT48K, the PCBM agglomerate size decreases with increased number density, which may arise from the decreased chain mobility at the annealing temperature, slowing the movement and organization of PCBM.

2.2. Photovoltaic Devices and Morphology. *2.2.1. Device Characteristics.* Photovoltaic devices were prepared using P3HTs mixed with PCBM (1:1 weight ratio) in a chlorobenzene solution. The thickness of the casted films was ~100 nm. "Preannealing" and "postannealing" thermal treatments were used ("preannealing" means annealing of the sample before electrode deposition; "postannealing" means annealing of the sample after electrode deposition). Both "preannealing" and "postannealing" enhance the device performance compared to that of the "as-spun" device.[22] To avoid the PCBM crystallization or aggregation noted above, a 5 min annealing time was used at 150 °C. From scanning force microscopy surface analysis (Figure S4 in the SI), postannealing led to rougher surfaces compared to preannealing. No large PCBM crystallization was seen in both cases. Detailed information for device fabrication is described in the experimental section. Table 2 summarizes the device performance. The "as-spun" devices showed a low short-circuit current (J_{sc}). The "preannealed" devices showed a much higher J_{sc}, but the open-circuit voltage (V_{oc}) decreased. "Postannealing" increases J_{sc}, V_{oc}, and the fill factor (FF). For the annealed devices (both pre- and postannealed), the large increase in J_{sc} can be attributed to the ordering or crystallization of P3HT and the segregation of PCBM.[56] The better performance of the "postannealed" device, as shown previously,[22] arises from an enrichment of PCBM at the cathode–active layer interface.

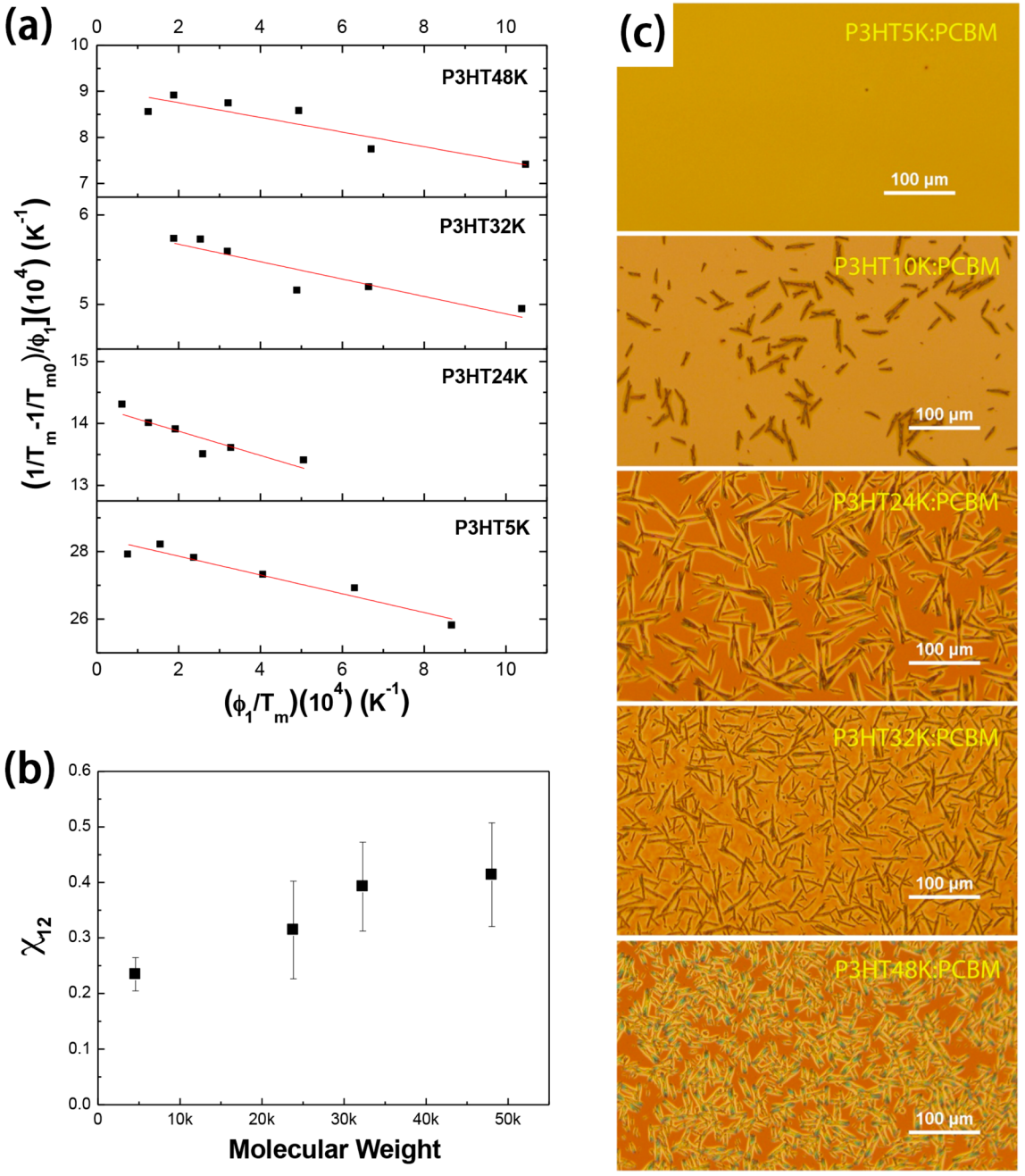

Figure 7. (a) Plot of $(1/T_m - 1/T_m^\circ)/\phi_1$ as a function of ϕ_1/T_m for the P3HT:PCBM mixture, where T_m is the melting point of the blends and T_m° is the equilibrium melting point of pure P3HT. (b) Interaction parameter χ_{12} between P3HT and PCBM at 150 °C obtained from melting point depression calculation. (c) Optical microscopic image of prolonged annealed P3HT:PCBM thin films.

Figure 8 shows the current–voltage (I–V) characteristics of the "postannealed" devices using P3HT where the MW varies from 5K to 48K. For P3HT5K, J_{sc} was much lower than that found for the high-MW polymers. This may arise from the weaker absorption and poor morphology. For a polymer with a shorter conjugation length, a slightly deeper HOMO energy level is observed, which corresponds to a larger V_{oc} in the device. This effect is seen in the "postannealed" devices. Morphology details also affect V_{oc}, mostly coming from the vertical segregation of the BHJ blends, which will change the cathode side contact and carrier transport throughout the film, explaining why the V_{oc} trend does not follow the energy level changes in PESA measurements in as-spun and preannealed devices. P3HT showing the best performance in our studies had a MW of 24K with the largest J_{sc} and an FF of 64%. Further increasing the MW resulted in a reduction in J_{sc}, FF, and the overall efficiency. The decrease in FF for the higher-MW blends (32K and 48K polymers) arises, more than likely, from a reduction in the chain mobility and an increase in the number of entanglements per chain, both of which will retard the ordering of P3HT. The vertical hole mobility across the device[20] for the "postannealed" P3HT:PCBM blends was determined from space charge limited current (SCLC) measurements using ITO/PEDOT:PSS/P3HT:PCBM blends/Au single carrier devices (Figure S5 in the SI). The vertical hole mobility was found to decrease with increasing

dx.doi.org/10.1021/am505283k | ACS Appl. Mater. Interfaces 2014, 6, 19876–19887

Table 2. Device Performance

		V_{oc} (V)	J_{sc} (mA/cm^2)	FF (%)	PCE (%)
P3HT5K	as-spun	0.60	1.43	34	0.29
	preanneal	0.45	6.24	34	0.96
	postanneal	0.66	3.33	61	1.35
P3HT10K	as-spun	0.57	2.60	25	0.37
	preanneal	0.47	8.32	44	1.73
	postanneal	0.63	8.42	48	2.53
P3HT24K	as-spun	0.55	1.02	30	0.17
	preanneal	0.38	7.72	47	1.38
	postanneal	0.59	9.01	64	3.42
P3HT32K	as-spun	0.44	0.93	29	0.12
	preanneal	0.39	6.73	39	1.04
	postanneal	0.56	8.03	52	2.38
P3HT48K	as-spun	0.45	1.08	29	0.14
	preanneal	0.42	6.03	36	0.92
	postanneal	0.57	8.18	47	2.22

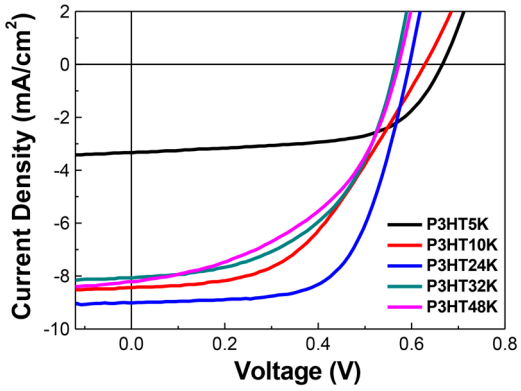

Figure 8. *I*–*V* curve of postannealed devices with aluminum as the cathode.

MW from 24K to 48K, which is consistent with the device results.

The results show that, under the standard conditions of device preparation, there is an optimum MW of ~20K for enhancing the efficiency of P3HT:PCBM. At this MW, the kinetics of P3HT crystallization and diffusion of PCBM away from the growth front are more effective, leading to segregated desirable phase-separated morphology. With increasing MW, the rate of crystallization of P3HT and diffusion of PCBM will decrease because of the increase in the viscosity of the system. While the miscibility presents a counterforce to phase separation at the lower MWs, it is seen to decrease with increasing MW. These competing, MW-dependent factors give rise to a morphology at intermediate MWs in which exciton generation, transport and dissociation, and charge transport to the electrodes are optimal. It should be noted that the current correlation of the structure–property relationship regarding MW is based on the spin coating and consequent thermal annealing process. If completely new processing methods are used, for example, using high-boiling-point solvents or additives, the morphology can be different from that of the current discussion.

2.2.2. Structure Order of P3HT in Blends. The ordering of P3HT in the blends was studied by GIXD. The as-cast P3HT:PCBM blends show P3HT crystal reflections, yet their order is poorer and crystal sizes are smaller compared to those of pure P3HT. Preannealed samples show enhanced (100) reflections (Figure S6 in the SI). The postannealed blends are of more interest in terms of performance. Figure 9a shows the

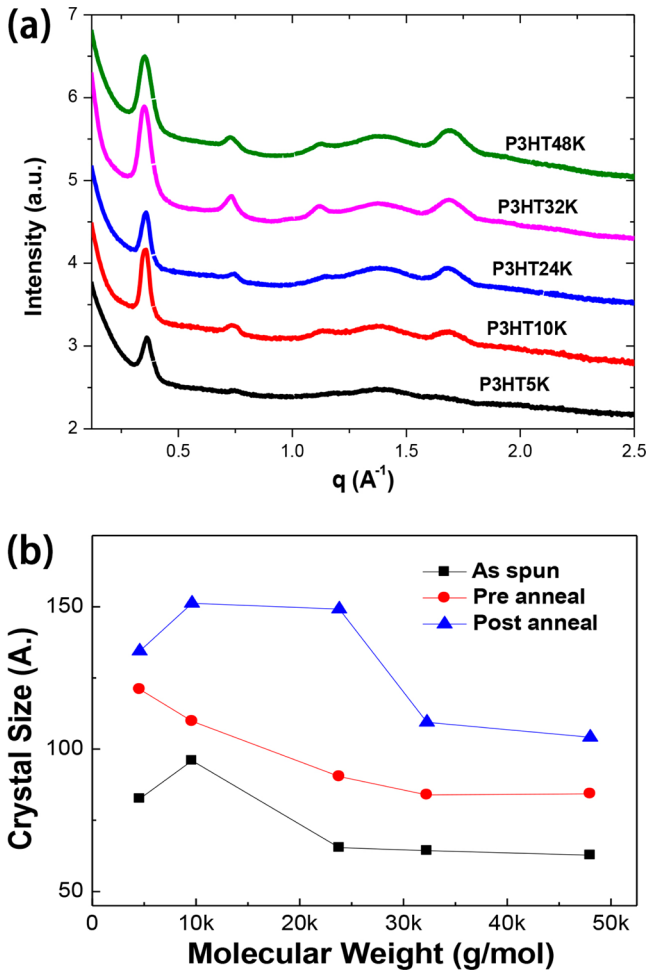

Figure 9. (a) Out-of-plane line profiles of postannealed blends. (b) Summary of the crystal size of the (100) peak in the out-of-plane direction.

out-of-plane GIXD of postannealed samples and the diffraction images as summarized in the SI (Figure S7). The (100) reflection and high orders are obvious for these samples. It can be seen that the azimuthal orientation of the (100) peak is quite broad. While the most intense region of the (100) diffraction ring appears in the out-of-plane direction, the in-plane direction also showed some intensity enhancement. This distribution of (100) chain packing indicates that edge-on crystals and face-on crystals both exist in the blends. Indeed, a diffusive (020) diffraction arc was observed in the out-of-plane direction. These results are quite different from those of preannealed P3HT:PCBM blends and could give rise to an enhancement in the efficiency. The areas of the (100) and (020) diffraction peaks are calculated, and the ratio of (020) peak versus (100) peak is plotted (Figure S5 in the SI). It is seen that P3HT24K:PCBM blends give the highest value. The π–π stacking in the out-of-plane direction can promote the vertical hole transport, which will balance the carrier transport in the BHJ active layer, leading to efficiency enhancement. This structural information is consistent with the device performance and SCLC mobility measurements. Figure 9b shows the (100) crystal size for blended samples. The "as-spun" thin films show

dx.doi.org/10.1021/am505283k | ACS Appl. Mater. Interfaces 2014, 6, 19876–19887

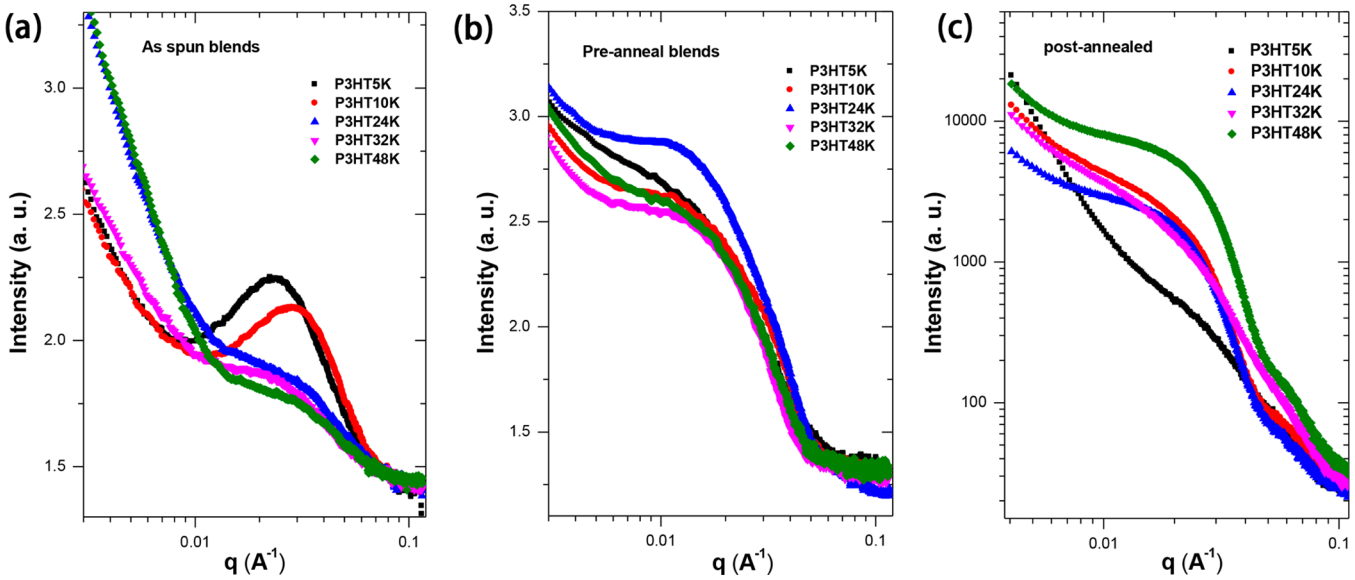

Figure 10. GISAXS of a P3HT:PCBM blend thin film with different posttreatment conditions in the in-plane direction: (a) as-spun blends; (b) preannealed blends; (c) postannealed blends at 150 °C for 5 min.

the smallest value for each MW because they are less ordered. The "preannealing" process, as would be expected, results in an increase in the crystal size. For P3HT5K, the crystal size is ∼125 Å. For P3HT32K and P3HT48K, the "preannealed" blends show a crystal size of ∼80 Å. The "postannealed" films show a larger crystal size in comparison to the "preannealed" films. It is unexpected that different annealing methods lead to such a big difference in the crystal size. It is expected that, in "postannealing" process, there are two contacts with the BHJ thin film. Also, PCBM has a higher surface energy, which will wet the surface readily. Thus, during "postannealing", the vertical redistribution of PCBM, its concentration enhancement at bottom and top contacted surfaces, will lead to reduction of the PCBM concentration in BHJ, thus resulting in larger P3HT crystals because the growth front is embedded with less PCBM. This increase in the crystal size in the out-of-plane direction, together with a more face-on orientation, an increase of FF, and efficiency of the devices, is expected.[11,57]

2.2.3. Lateral Phase Separation. While the crystalline structure of conjugated polymer plays an important role in device function, the lateral phase separation, which determines the phase size and donor−acceptor interfacial areas, is more critical in understanding the morphology−device function relationship. GISAXS was used to assess the in-plane density correlation in postannealed thin film blends of P3HT:PCBM.[47,58] Figure 10a shows GISAXS of the "as-spun" films. The P3HT5K:PCBM blends show a well-defined peak centered at 0.025 $Å^{-1}$, corresponding to a spacing of 25 nm. P3HT10K:PCBM blends show a peak at 0.031 $Å^{-1}$, corresponding to a spacing of 20 nm. For higher-MW samples, a very weak shoulder is seen at ∼0.31 $Å^{-1}$. This phase separation most likely arises from crystallization of the shorter P3HT chains during the solvent evaporation process. For higher-MW P3HTs, the lower chain mobility and chain entanglements slow the kinetics of ordering and, consequently, phase separation. This can be the origin of the lower device efficiency of the as-spun devices. Figure 10b shows GISAXS of "preannealed" P3HT:PCBM blends. All samples show a broad shoulder at ∼0.16 $Å^{-1}$, corresponding to a spacing of ∼40 nm. In comparison to the "as-spun" samples, the domain size has increased significantly. For the more efficient, postannealed blends, P3HT10K to P3HT48K shows a similar shoulder around 0.22 $Å^{-1}$ (shown in Figure 10c), giving a spacing of ∼28 nm. For P3HT5K, the shoulder is weak, and there is a sharp upturn of the intensity in the low-q region, indicating that a large-sized structure exists within the film that could be the origin of the lower efficiency. From these data, we can see that the "preannealing" is more efficient in driving the lateral phase separation. Thermal annealing of different times for P3HT24K:PCBM blends was also investigated (Figure S8 in the SI). The change in the scattering profiles showed the evolution of morphology, which also indicates that the thermally induced BHJ in this system is also a kinetically trapped structure.

Transmission resonant soft X-ray scattering (RSoXS) was used to investigate the morphology of the postannealed P3HT:PCBM thin films, taking advantage of the ability to tune the contrast by changing the energy of the incident X-rays and the longer wavelengths, allowing access to much lower q or larger size scales.[59,60] The RSoXS studies primarily focused on postannealed samples because these are the most important for device fabrication, and the as-spun samples were well-mixed and did not have well-developed interferences at the size scales probed by RSoXS. With RSoXS, the beam energy can be tuned to resonant edges of typical bond structures that impart chemical sensitivity. We used 284.2 eV photons to carry out the scattering experiment, which is at the carbon K-edge so as to probe the PCBM-rich structure.[61] The scattering profiles of the postannealed blends are shown in Figure 11 (due to the difficulties in the sample preparation, the P3HT5K blends were not studied). For P3HT10K blends, a diffuse maximum at 0.07 nm^{-1} is observed, giving a spacing of 88 nm. P3HT24K blends had a sharp peak at 0.09 nm^{-1}, corresponding to a 70 nm spacing. This is larger than in the GISAXS results and similar to the EFTEM findings of Drummy et al.[62] P3HT32K blends show a similar peak at 0.09 nm^{-1}, but the peak intensity is much lower. P3HT48K blends show a broad peak ranging from 0.09 to 0.2 nm^{-1} (a spacing from 70 to 31 nm). The RSoXS spacing is much larger than that observed by GISAXS. The differences seen by RSoXS and GISAXS clearly show that the

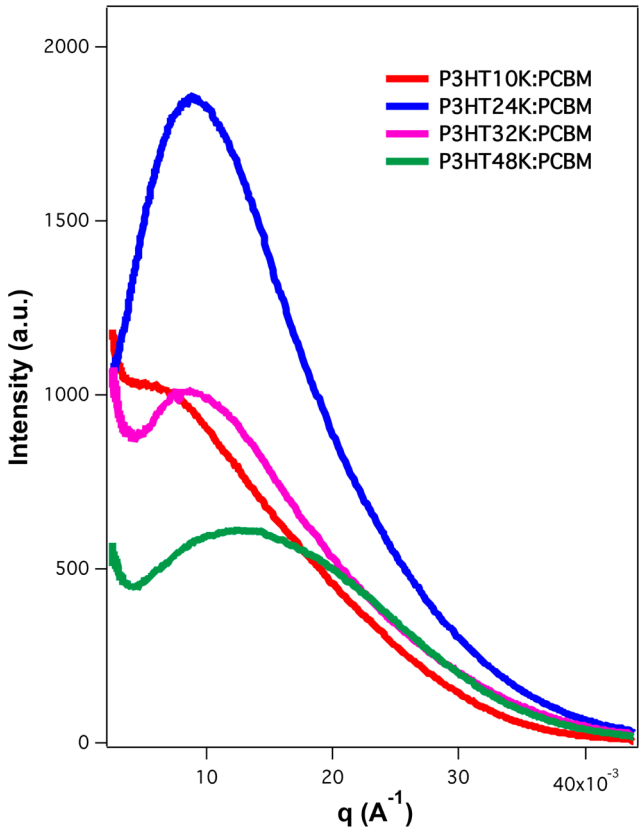

Figure 11. Transition RSoXS of postannealed P3HT:PCBM thin film blends.

blended thin film morphology cannot be described by one length scale and there must be at least two different size-scale structures in the postannealed thin film. This finding is similar to our previous observations on low-band-gap polymers, where a multilength-scaled morphology was found.[63−65] While in the RSoXS experiments the contrast can be tuned with the energy used, the scattering interferences observed reflect variation in the composition of the components, with a strong interference arising from the separation distance between P3HT crystals. The combined results of GISAXS and RSoXS reflect a morphology comprised of a network of P3HT crystals forming a meshlike structure with a characteristic mesh size of ∼70−90 nm. Inside the mesh, there is a distinctly different size-scale morphology of a much smaller size. The more pronounced the mesh structure, the better is the device performance, as shown in P3HT24K:PCBM blend samples in which a much stronger scattering intensity is recorded, indicating a better defined structure.

3. CONCLUSION

In conclusion, we have synthesized a series of P3HTs with well-defined MWs and PDIs. The physical properties and morphologies in thin films of these polymers and their blends with PCBM were investigated. All of the polymers showed similar absorption profiles. Higher-MW polymers more easily aggregate under bad solvent conditions. The kinetics of crystallization in a high-MW polymer is slowed in the thin-film casting process or thermal annealing processes because of the lower chain mobility. An unusual crystal lattice expansion behavior under heating was observed, which indicates that at 60 °C an enhancement in the $\pi-\pi$ stacking occurs. In devices, the best performance was found for an intermediate-MW P3HT. Morphology with two size-scale domains was observed by using different scattering methods. Together with absorption and mobility measurements, the results indicate that the multiple kinetic processes involved in generation of the morphology in the thin-film active layer, specifically the ordering of P3HT, phase segregation of PCBM, and orientation of P3HT in the thin film (all of which are influenced by the chain mobility) and the miscibility of P3HT with PCBM and the casting solvent (thermodynamics), give rise to MW dependence of the morphology. The interplay between these kinetic and thermodynamic parameters results in an intermediate MW being best-suited for producing the morphology with the best performance in photovoltaic devices.

4. EXPERIMENTAL SECTION

Regioregular poly(3-hexylthiophene)s (P3HTs) were synthesized by the GRIM method. All reactions were performed under an inert nitrogen atmosphere. Tetrahydrofuran was distilled before use. The polymerization was carried out for approximately 2 h. When the reaction was complete, a methanol (MeOH)/HCl solution (20% HCl) was added to quench. Then additional MeOH was added, and precipitated polymers were collected and subjected to Soxhlet extraction. For P3HT5K and -10K, MeOH and acetone were used consecutively as extraction solvents; each step required more than 6 h. For P3HT24K and -32K, after MeOH and acetone extraction, hexane was further used to extract for an additional 6 h. For P3HT48K, extractions were consecutively carried out with MeOH, acetone, hexane, and dichloromethane. When all of these steps were completed, chloroform was used to wash the remaining polymers, reprecipitated, collected, dried, and stored in a nitrogen box. ^{1}H NMR characterization was performed on a Bruker 300 MHz NMR station. Gel permeation chromatography (GPC) was performed on an Agilent GPC system with a refractive index detector using chloroform as the eluent and polystyrene as the standard. The PESA measurements were performed using a RKI AC2.

[6,6]-Phenyl-C61-butyric acid methyl ester (PCBM) was obtained from American Dye Source. The indium tin oxide (ITO)-coated glass substrates (20 ± 5 Ω/□) were purchased from Thin Film Devices Inc., cleaned through ultrasonic treatment in detergent, deionized water, acetone, and isopropyl alcohol, and then dried in an oven overnight. PEDOT:PSS (Baytron P VP A1 4083; ∼35 nm) was spin-coated onto ultraviolet ozone-treated ITO substrates. After annealing at 150 °C for 30 min in air, the substrates were transferred to a glovebox. The P3HT (10 mg):PCBM (10 mg)/1 mL of chlorobenzene solution was spin-coated on top of the PEDOT:PSS layer. The thickness of the film was ∼90−100 nm (KLA-TENCOR Alpha-Step IQ surface profiler). A 100-nm-thick aluminum cathode was deposited (area 6 mm^2) on the active layer under high vacuum (2 × 10^{-4} Pa) using a thermal evaporator. For thermal annealing, spin-coated films or completed devices were placed directly on a digitally controlled hot plate and heated to 150 °C for the desired time. All $I-V$ characteristics were measured under simulated AM1.5G irradiation (100 mW/cm^2) using a xenon-lamp-based Newport 91160 300-W solar simulator. A xenon lamp equipped with an AM1.5G filter was used as the white-light source. The light intensity was adjusted with an NREL-calibrated silicon solar cell with a KG-5 filter.

Thin-film samples for property characterization were prepared on silicon substrates covered with PEDOT:PSS. BHJ thin films were directly cast onto substrates and processed with various conditions. For preannealed samples, those samples were directly annealed under a nitrogen atmosphere. For postannealed samples, the top electrode was first thermally evaporated onto BHJ layers and subsequently annealed. After that, the aluminum electrode was removed by dissolving it in diluted copper chloride aqueous solutions.

GIXD measurements were performed on a Beamline 7.3.3 at ALS, LBNL. The experimental setup and sample cell were designed for the surface studies on thin films. An X-ray beam impinged onto the sample

at a grazing angle above and below the critical angle of the polymer film (α_c = 0.18) but below the critical angle of the silicon substrate (α_c = 0.28). The wavelength of X-rays used was 1.240 Å, and the scattered intensity was detected by using a two-dimensional charge-coupled-device (CCD) camera with image sizes of 2304 × 2304 pixels or a PILATUS 1 M detector. Transition WAXS was done in the NSLS Brookhaven National Laboratory using a Mar CCD detector.

RSoXS experiments were performed at Beamline 11.0.1.2 at ALS, LBNL. RSoXS experiments were performed using transmission geometry. Samples were prepared by floating thin films onto a Si_3N_4 membrane (5 mm × 5 mm) with a window size of 1.5 mm × 1.5 mm. Monochromatic soft X-rays near the carbon K-edge was used for the scattering measurement. The energy resolution was ∼0.1 eV. The beam size on the sample position was ∼100 μm × 100 μm. The sample detector distance was ∼100 mm. A Princeton Instrument CCD (PI-MTE) was the detector. 2048 × 2048 and 13.5 μm × 13.5 μm pixel size were used.

■ ASSOCIATED CONTENT

Supporting Information

Experimental details and part of the characterization results. This material is available free of charge via the Internet at http://pubs.acs.org.

■ AUTHOR INFORMATION

Corresponding Author

*E-mail: Russell@mail.pse.umass.edu.

Notes

The authors declare no competing financial interest.

■ ACKNOWLEDGMENTS

This work was supported by the Department of Energy (DOE) supported the Energy Frontier Research Center at the University of Massachusetts (DOE Grant DE-DE-SC0001087). Portions of this research were performed at the Advanced Light Source, Berkeley National Laboratory, which was supported by the DOE, Office of Science, and Office of Basic Energy Sciences. We also thank Y. Gu, X. Shen, A. Hexemer, and A. Young for assistance with some of the experiments. J.W.P.H. acknowledges Texas Instruments Distinguished Chair in Nanoelectronics.

■ REFERENCES

(1) Brabec, C. J.; Gowrisanker, S.; Halls, J. J. M.; Laird, D.; Jia, S.; Williams, S. P. Polymer−Fullerene Bulk-Heterojunction Solar Cells. *Adv. Mater.* **2010**, *22*, 3839−3856.

(2) Yu, G.; Gao, J.; Hummelen, J.; Wudl, F.; Heeger, A. Polymer Photovoltaic Cells: Enhanced Efficiencies via a Network of Internal Donor−Acceptor Heterojunctions. *Science* **1995**, *270*, 1789−1791.

(3) Thompson, B. C.; Fréchet, J. M. J. Polymer−Fullerene Composite Solar Cells. *Angew. Chem., Int. Ed.* **2008**, *47*, 58−77.

(4) Liu, F.; Gu, Y.; Jung, J. W.; Jo, W. H.; Russell, T. P. On the Morphology of Polymer-Based Photovoltaics. *J. Polym. Sci., Part B: Polym. Phys.* **2012**, *50*, 1018−1044.

(5) Liu, F.; Gu, Y.; Shen, X.; Ferdous, S.; Wang, H.-W.; Russell, T. P. Characterization of the Morphology of Solution-Processed Bulk Heterojunction Organic Photovoltaics. *Prog. Polym. Sci.* **2013**, *38*, 1990−2052.

(6) Shaw, P. E.; Ruseckas, A.; Samuel, I. D. W. Exciton Diffusion Measurements in Poly(3-Hexylthiophene). *Adv. Mater.* **2008**, *20*, 3516−3520.

(7) Campoy-Quiles, M.; Ferenczi, T.; Agostinelli, T.; Etchegoin, P. G.; Kim, Y.; Anthopoulos, T. D.; Stavrinou, P. N.; Bradley, D. D. C.; Nelson, J. Morphology Evolution via Self-Organization and Lateral and Vertical Diffusion in Polymer: Fullerene Solar Cell Blends. *Nat. Mater.* **2008**, *7*, 158−164.

(8) Ruderer, M. A.; Guo, S.; Meier, R.; Chiang, H.-Y.; Körstgens, V.; Wiedersich, J.; Perlich, J.; Roth, S. V.; Müller-Buschbaum, P. Solvent-Induced Morphology in Polymer-Based Systems for Organic Photovoltaics. *Adv. Funct. Mater.* **2011**, *21*, 3382−3391.

(9) Shaheen, S. E.; Brabec, C. J.; Sariciftci, N. S.; Padinger, F.; Fromherz, T.; Hummelen, J. C. 2.5% Efficient Organic Plastic Solar Cells. *Appl. Phys. Lett.* **2001**, *78*, 841−843.

(10) Li, G.; Yao, Y.; Yang, H.; Shrotriya, V.; Yang, G.; Yang, Y. "Solvent Annealing" Effect in Polymer Solar Cells Based on Poly(3-Hexylthiophene) and Methanofullerenes. *Adv. Funct. Mater.* **2007**, *17*, 1636−1644.

(11) Mihailetchi, V. D.; Xie, H.; de Boer, B.; Popescu, L. M.; Hummelen, J. C.; Blom, P. W. M.; Koster, L. J. A. Origin of the Enhanced Performance in Poly(3-Hexylthiophene): [6,6]-Phenyl-C_{61}-Butyric Acid Methyl Ester Solar Cells Upon Slow Drying of the Active Layer. *Appl. Phys. Lett.* **2006**, *89*, 012107.

(12) Li, G.; Shrotriya, V.; Huang, J.; Yao, Y.; Moriarty, T.; Keith, E.; Yang, Y. High-Efficiency Solution Processable Polymer Photovoltaic Cells by Self-Organization of Polymer Blends. *Nat. Mater.* **2005**, *4*, 864−868.

(13) Moule, A. J.; Meerholz, K. Controlling Morphology in Polymer−Fullerene Mixtures. *Adv. Mater.* **2008**, *20*, 240−245.

(14) Yao, Y.; Hou, J.; Xu, Z.; Li, G.; Yang, Y. Effects of Solvent Mixtures on the Nanoscale Phase Separation in Polymer Solar Cells. *Adv. Funct. Mater.* **2008**, *18*, 1783−1789.

(15) Chen, F.-C.; Tseng, H.-C.; Ko, C.-J. Solvent Mixtures for Improving Device Efficiency of Polymer Photovoltaic Devices. *Appl. Phys. Lett.* **2008**, *92*, 103316.

(16) Chen, H.-Y.; Yang, H.; Yang, G.; Sista, S.; Zadoyan, R.; Li, G.; Yang, Y. Fast-Grown Interpenetrating Network in Poly(3-Hexylthiophene): Methanofullerenes Solar Cells Processed with Additive. *J. Phys. Chem. C* **2009**, *113*, 7946−7953.

(17) Lee, J. K.; Ma, W. L.; Brabec, C. J.; Yuen, J.; Moon, J. S.; Kim, J. Y.; Lee, K.; Bazan, G. C.; Heeger, A. J. Processing Additives for Improved Efficiency from Bulk Heterojunction Solar Cells. *J. Am. Chem. Soc.* **2008**, *130*, 3619−3623.

(18) Peet, J.; Kim, J. Y.; Coates, N. E.; Ma, W. L.; Moses, D.; Heeger, A. J.; Bazan, G. C. Efficiency Enhancement in Low-Bandgap Polymer Solar Cells by Processing with Alkane Dithiols. *Nat. Mater.* **2007**, *6*, 497−500.

(19) Pivrikas, A.; Stadler, P.; Neugebauer, H.; Sariciftci, N. S. Substituting the Postproduction Treatment for Bulk-Heterojunction Solar Cells Using Chemical Additives. *Org. Electron.* **2008**, *9*, 775−782.

(20) Mihailetchi, V. D.; Xie, H. X.; de Boer, B.; Koster, L. J. A.; Blom, P. W. M. Charge Transport and Photocurrent Generation in Poly(3-Hexylthiophene): Methanofullerene Bulk-Heterojunction Solar Cells. *Adv. Funct. Mater.* **2006**, *16*, 699−708.

(21) Ma, W.; Yang, C.; Gong, X.; Lee, K.; Heeger, A. J. Thermally Stable, Efficient Polymer Solar Cells with Nanoscale Control of the Interpenetrating Network Morphology. *Adv. Funct. Mater.* **2005**, *15*, 1617−1622.

(22) Chen, D.; Nakahara, A.; Wei, D.; Nordlund, D.; Russell, T. P. P3HT/PCBM Bulk Heterojunction Organic Photovoltaics: Correlating Efficiency and Morphology. *Nano Lett.* **2011**, *11*, 561−567.

(23) Orimo, A.; Masuda, K.; Honda, S.; Benten, H.; Ito, S.; Ohkita, H.; Tsuji, H. Surface Segregation at the Aluminum Interface of Poly(3-Hexylthiophene)/Fullerene Solar Cells. *Appl. Phys. Lett.* **2010**, *96*, 043305.

(24) Yang, X.; Loos, J.; Veenstra, S. C.; Verhees, W. J. H.; Wienk, M. M.; Kroon, J. M.; Michels, M. A. J.; Janssen, R. A. J. Nanoscale Morphology of High-Performance Polymer Solar Cells. *Nano Lett.* **2005**, *5*, 579−583.

(25) Zhao, Y.; Xie, Z.; Qu, Y.; Geng, Y.; Wang, L. Solvent-Vapor Treatment Induced Performance Enhancement of Poly(3-Hexylthiophene): Methanofullerene Bulk-Heterojunction Photovoltaic Cells. *Appl. Phys. Lett.* **2007**, *90*, 043504.

(26) Li, H.; Tang, H.; Li, L.; Xu, W.; Zhao, X.; Yang, X. Solvent-Soaking Treatment Induced Morphology Evolution in P3HT/PCBM Composite Films. *J. Mater. Chem.* **2011**, *21*, 6563−6568.

(27) Park, J. H.; Kim, J. S.; Lee, J. H.; Lee, W. H.; Cho, K. Effect of Annealing Solvent Solubility on the Performance of Poly(3-Hexylthiophene)/Methanofullerene Solar Cells. *J. Phys. Chem. C* **2009**, *113*, 17579−17584.
(28) Chen, F.-C.; Ko, C.-J.; Wu, J.-L.; Chen, W.-C. Morphological Study of P3HT:PCBM Blend Films Prepared Through Solvent Annealing for Solar Cell Applications. *Sol. Energy Mater. Sol. Cells* **2010**, *94*, 2426−2430.
(29) Hiorns, R. C.; de Bettignies, R.; Leroy, J.; Bailly, S.; Firon, M.; Sentein, C.; Khoukh, A.; Preud'homme, H.; Dagron-Lartigau, C. High Molecular Weights, Polydispersities, and Annealing Temperatures in the Optimization of Bulk-Heterojunction Photovoltaic Cells Based on Poly(3-Hexylthiophene) or Poly(3-Butylthiophene). *Adv. Funct. Mater.* **2006**, *16*, 2263−2273.
(30) Müller, C.; Wang, E.; Andersson, L. M.; Tvingstedt, K.; Zhou, Y.; Andersson, M. R.; Inganäs, O. Influence of Molecular Weight on the Performance of Organic Solar Cells Based on a Fluorene Derivative. *Adv. Funct. Mater.* **2010**, *20*, 2124−2131.
(31) Schilinsky, P.; Asawapirom, U.; Scherf, U.; Biele, M.; Brabec, C. J. Influence of the Molecular Weight of Poly(3-Hexylthiophene) on the Performance of Bulk Heterojunction Solar Cells. *Chem. Mater.* **2005**, *17*, 2175−2180.
(32) Bijleveld, J. C.; Zoombelt, A. P.; Mathijssen, S. G. J.; Wienk, M. M.; Turbiez, M.; de Leeuw, D. M.; Janssen, R. A. J. Poly-(Diketopyrrolopyrrole−Terthiophene) for Ambipolar Logic and Photovoltaics. *J. Am. Chem. Soc.* **2009**, *131*, 16616−16617.
(33) Ma, W.; Kim, J. Y.; Lee, K.; Heeger, A. J. Effect of the Molecular Weight of Poly(3-Hexylthiophene) on the Morphology and Performance of Polymer Bulk Heterojunction Solar Cells. *Macromol. Rapid Commun.* **2007**, *28*, 1776−1780.
(34) Wu, Z.; Petzold, A.; Henze, T.; Thurn-Albrecht, T.; Lohwasser, R. H.; Sommer, M.; Thelakkat, M. Temperature and Molecular Weight Dependent Hierarchical Equilibrium Structures in Semiconducting Poly(3-Hexylthiophene). *Macromolecules* **2010**, *43*, 4646−4653.
(35) Zen, A.; Saphiannikova, M.; Neher, D.; Grenzer, J.; Grigorian, S.; Pietsch, U.; Asawapirom, U.; Janietz, S.; Scherf, U.; Lieberwirth, I.; et al. Effect of Molecular Weight on the Structure and Crystallinity of Poly(3-Hexylthiophene). *Macromolecules* **2006**, *39*, 2162−2171.
(36) Kline, R. J.; McGehee, M. D.; Kadnikova, E. N.; Liu, J.; Fréchet, J. M. J.; Toney, M. F. Dependence of Regioregular Poly(3-Hexylthiophene) Film Morphology and Field-Effect Mobility on Molecular Weight. *Macromolecules* **2005**, *38*, 3312−3319.
(37) Moet, D. J. D.; Lenes, M.; Kotlarski, J. D.; Veenstra, S. C.; Sweelssen, J.; Koetse, M. M.; de Boer, B.; Blom, P. W. M. Impact of Molecular Weight on Charge Carrier Dissociation in Solar Cells From a Polyfluorene Derivative. *Org. Electron.* **2009**, *10*, 1275−1281.
(38) Joshi, S.; Grigorian, S.; Pietsch, U. X-Ray Structural and Crystallinity Studies of Low and High Molecular Weight Poly(3-Hexylthiophene). *Phys. Status Solidi A* **2008**, *205*, 488−496.
(39) Osaka, I.; McCullough, R. D. Advances in Molecular Design and Synthesis of Regioregular Polythiophenes. *Acc. Chem. Res.* **2008**, *41*, 1202−1214.
(40) Sivula, K.; Luscombe, C. K.; Thompson, B. C.; Fréchet, J. M. J. Enhancing the Thermal Stability of Polythiophene:Fullerene Solar Cells by Decreasing Effective Polymer Regioregularity. *J. Am. Chem. Soc.* **2006**, *128*, 13988−13989.
(41) Iovu, M. C.; Sheina, E. E.; Gil, R. R.; McCullough, R. D. Experimental Evidence for the Quasi-Living Nature of the Grignard Metathesis Method for the Synthesis of Regioregular Poly(3-Alkylthiophenes). *Macromolecules* **2005**, *38*, 8649−8656.
(42) Monson, T. C.; Lloyd, M. T.; Olson, D. C.; Lee, Y.-J.; Hsu, J. W. P. Photocurrent Enhancement in Polythiophene- and Alkanethiol-Modified ZnO Solar Cells. *Adv. Mater.* **2008**, *20*, 4755−4759.
(43) Kayunkid, N.; Uttiya, S.; Brinkmann, M. Structural Model of Regioregular Poly(3-Hexylthiophene) Obtained by Electron Diffraction Analysis. *Macromolecules* **2010**, *43*, 4961−4967.
(44) Onoda, M.; Tada, K.; Nakayama, H. Electronic Energy States of Organic Interfaces Studied by Low-Energy Ultraviolet Photoemission Spectroscopy. *J. Appl. Phys.* **1999**, *86*, 2110−2115.
(45) Uda, M.; Nakagawa, Y.; Yamamoto, T.; Kawasaki, M.; Nakamura, A.; Saito, T.; Hirose, K. Successive Change in Work Function of Al Exposed to Air. *J. Electron Spectrosc. Relat. Phenom.* **1998**, *88*−*91*, 767−771.
(46) Malik, S.; Nandi, A. K. Crystallization Mechanism of Regioregular Poly(3-Alkyl Thiophene)S. *J. Polym. Sci., Part B: Polym. Phys.* **2002**, *40*, 2073−2085.
(47) Chiu, M.-Y.; Jeng, U.-S.; Su, C.-H.; Liang, K. S.; Wei, K.-H. Simultaneous Use of Small- and Wide-Angle X-Ray Techniques to Analyze Nanometerscale Phase Separation in Polymer Heterojunction Solar Cells. *Adv. Mater.* **2008**, *20*, 2573−2578.
(48) Yuan, Y.; Zhang, J.; Sun, J. Effect of Solvent Evaporation Rate on Order-to-Disorder Phase Transition Behavior of Regioregular Poly(3-Butylthiophene). *Macromolecules* **2011**, *44*, 6128−6135.
(49) Hashimoto, T.; Saijo, K.; Kosc, M.; Kawai, H.; Wasiak, A.; Ziabicki, A. Oriented Crystallization of Cross-Linked Polybutadiene Rubber. 2. Small-Angle and Wide-Angle X-Ray Scattering Studies of Crystal Orientation. *Macromolecules* **1985**, *18*, 472−482.
(50) Flory, P. J. *Principles of Polymer Chemistry*; Cornell University Press: Ithaca, NY, 1953.
(51) Flory, P. J. Thermodynamics of Crystallization in High Polymers. IV. a Theory of Crystalline States and Fusion in Polymers, Copolymers, and Their Mixtures with Diluents. *J. Chem. Phys.* **1949**, *17*, 223−240.
(52) Nishi, T.; Wang, T. Melting Point Depression and Kinetic Effects of Cooling on Crystallization in Poly(Vinylidene Fluoride)−Poly(Methyl Methacrylate) Mixtures. *Macromolecules* **1975**, *8*, 909−915.
(53) Simek, L.; Dostal, J.; Bohdanecky, M. Morphological Factor in the Melting Point Depression of Polypropylene by Alkanes. *Polymer* **2001**, *42*, 8897−8900.
(54) Chen, D.; Liu, F.; Wang, C.; Nakahara, A.; Russell, T. P. Bulk Heterojunction Photovoltaic Active Layers via Bilayer Interdiffusion. *Nano Lett.* **2011**, *11*, 2071−2078.
(55) Chang, L.; Lademann, H. W. A.; Bonekamp, J.-B.; Meerholz, K.; Moulé, A. J. Effect of Trace Solvent on the Morphology of P3HT:PCBM Bulk Heterojunction Solar Cells. *Adv. Funct. Mater.* **2011**, *21*, 1779−1787.
(56) Kiel, J.; Eberle, A.; Mackay, M. Nanoparticle Agglomeration in Polymer-Based Solar Cells. *Phys. Rev. Lett.* **2010**, *105*, 168701.
(57) Ballantyne, A.; Chen, L.; Dane, J.; Hammant, T.; Braun, F.; Heeney, M.; Duffy, W.; McCulloch, I.; Bradley, D. D. C.; Nelson, J. The Effect of Poly(3-Hexylthiophene) Molecular Weight on Charge Transport and the Performance of Polymer:Fullerene Solar Cells. *Adv. Funct. Mater.* **2008**, *18*, 2373−2380.
(58) Liao, H.-C.; Tsao, C.-S.; Lin, T.-H.; Chuang, C.-M.; Chen, C.-Y.; Jeng, U.-S.; Su, C.-H.; Chen, Y.-F.; Su, W.-F. Quantitative Nanoorganized Structural Evolution for a High Efficiency Bulk Heterojunction Polymer Solar Cell. *J. Am. Chem. Soc.* **2011**, *133*, 13064−13073.
(59) Gann, E.; Young, A. T.; Collins, B. A.; Yan, H.; Nasiatka, J.; Padmore, H. A.; Ade, H.; Hexemer, A.; Wang, C. Soft X-Ray Scattering Facility at the Advanced Light Source with Real-Time Data Processing and Analysis. *Rev. Sci. Instrum.* **2012**, *83*, 045110.
(60) Wang, C.; Lee, D. H.; Hexemer, A.; Kim, M. I.; WWei, Z.; Hasegawa, H.; Ade, H.; Russell, T. P. Defining the Nanostructured Morphology of Triblock Copolymers Using Resonant Soft X-Ray Scattering. *Nano Lett.* **2011**, *11*, 3906−3911.
(61) Collins, B. A.; Gann, E.; Guignard, L.; He, X.; McNeill, C. R.; Ade, H. Molecular Miscibility of Polymer−Fullerene Blends. *J. Phys. Chem. Lett.* **2010**, *1*, 3160−3166.
(62) Drummy, L. F.; Davis, R. J.; Moore, D. L.; Durstock, M.; Vaia, R. A.; Hsu, J. W. P. Molecular-Scale and Nanoscale Morphology of P3HT:PCBM Bulk Heterojunctions: Energy-Filtered TEM and Low-Dose HREM. *Chem. Mater.* **2011**, *23*, 907−912.
(63) Liu, F.; Gu, Y.; Wang, C.; WWei, Z.; Chen, D.; Briseno, A. L.; Russell, T. P. Efficient Polymer Solar Cells Based on a Low Bandgap Semi-Crystalline DPP Polymer−PCBM Blends. *Adv. Mater.* **2012**, *24*, 3947−3951.

(64) Gu, Y.; Wang, C.; Russell, T. P. Multi-Length-Scale Morphologies in PCPDTBT/PCBM Bulk-Heterojunction Solar Cells. *Adv. Energy Mater.* **2012**, *2*, 683−690.
(65) Chen, W.; Xu, T.; He, F.; Wang, W.; Wang, C.; Strzalka, J.; Liu, Y.; Wen, J.; Miller, D. J.; Chen, J.; et al. Hierarchical Nanomorphologies Promote Exciton Dissociation in Polymer/Fullerene Bulk Heterojunction Solar Cells. *Nano Lett.* **2011**, *11*, 3707−3713.